

Lightweight Gradient Descent Optimization for Mitigating Hardware Imperfections in RIS Systems

Pedro H. C. de Souza^{1*}, Luiz A. M. Pereira^{1†},
 Faustino R. Gómez^{1†}, Elsa M. Materón^{1†},
 Jorge Ricardo Mejía-Salazar^{1†}, Luciano Mendes^{1†}

^{1*}Department, National Institute of Telecommunications - Inatel, Av.
 João de Camargo, 510, Santa Rita do Sapucaí, 37536-001, Minas
 Gerais, Brazil.

*Corresponding author(s). E-mail(s): pedro.carneiro@dtel.inatel.br;
 Contributing authors: luiz.melo@inatel.br;
faustino.gomez@posdoc.inatel.br; elsa.materon@posdoc.inatel.br;
jrmejia@inatel.br; luciano@inatel.br;

[†]These authors contributed equally to this work.

Abstract

Ongoing discussions about the future of wireless communications are reaching a turning point as standardization activities for the sixth generation of mobile networks (6G) become more mature. New technologies must now face renewed scrutiny by the industry and academia in order to be ready for deployment in the near future. Recently, reconfigurable intelligent surfaces (RISs) gained attention as a promising solution for improving the propagation conditions of signal transmission in general. The RIS is a planar array of tunable resonant elements designed to dynamically and precisely manipulate the reflection of incident electromagnetic waves. However, the physical structure of the RIS and its components may be subject to practical limitations and imperfections. It is imperative that the hardware imperfections (HWIs) associated with the RIS be analyzed, so that it remains a feasible technology from a practical standpoint. Moreover, solutions for mitigating the HWIs must be considered, as is discussed in this work. More specifically, we introduce a gradient descent optimization for mitigating HWIs in RIS-aided wideband communication systems. Numerical results show that the proposed optimization is able to compensate for HWIs such as the phase-shift noise (PSN) and RIS surface deformations.

Keywords: reconfigurable intelligent surfaces, hardware imperfections, gradient descent optimization, phase-shift noise

1 Introduction

With the consolidation of the fifth generation of mobile networks (5G) and the ongoing standardization efforts in the sixth generation of mobile networks (6G), emerging technologies such as reconfigurable intelligent surfaces (RISs) have become the focus of studies in industry and academia alike [1, 2]. The RIS is typically envisioned as a planar surface, built with passive elements, such as tunable resonant elements with adjustable impedance values (phase-shifts) [3]. This enables the RIS elements or reflectors, to act as independent wave scatterers [4]. In other words, a well positioned RIS between a transmitter and receiver can create additional paths for the signal propagation. Consequently, favorable propagation conditions for the signal transmission can be established even in scenarios where the transmitter have a non-line-of-sight (NLOS) in relation to the receiver.

There are several works available in the literature about RIS systems. Most of them are usually concerned with (idealized) system level operation and metrics, such as the maximization of channel capacity at the receiver [5]. On the other hand, the authors of [6] investigate a proposed RIS hardware to the extent where the design of each reflector element is detailed, mainly to discuss the wave propagation properties on such elements. However, works that can balance a system level analysis of RIS systems, alongside with practical considerations brought by hardware imperfections (HWIs), are more scarce in the literature. In line with that, [7], for example, studies the beamforming properties of a RIS in a experimental setting. From that, the authors of [7] then build an analytical model in order to evaluate the impact of different HWIs on the RIS performance. Alternatively, the work [8] incorporates noise into the proposed method for configuring the RIS.

Recently, instead of only analyzing the impact of HWIs on the RIS, authors of [9] proposed an optimization method to actively compensate for them. It is based on the gradient descent, which attempts to compensate for phase-shift errors and amplitude coupling at each RIS reflector. Therefore, in this work we build upon [9] in order to propose a method for mitigating the impact of HWIs on the RIS performance. However, in this work we leverage numerical tools and automatic differentiation as a means to compute the gradient descent. This contrasts to the approach taken by the authors of [9], where the expression for calculating the gradients is derived analytically, requiring the knowledge a priori of the distributions that describe the behavior of the HWIs. Furthermore, the method of [9] also requires a numerical computation of integrals, thus a closed-form solution is at any rate not provided.

In this work, we consider the effects of the phase-shift noise (PSN) and RIS surface deformations in the context of signal transmission, and reflection, over wideband communication channels, by using the orthogonal frequency division multiplex (OFDM) system. Therefore, the main contributions of this work can be established as follows:

- RIS phase-shift compensation with no prior knowledge of HWIs distributions;
- Metrics based on the system's average behavior [8, 9] are not required;
- The effects of surface deformations on the RIS performance are investigated;
- The gradient descent is computed considering multiple OFDM subcarriers.

Moreover, we also provide experimental results regarding the RIS electromagnetic response under surface deformations. These results support the findings discussed in this work, highlighting the importance of modeling hardware imperfections in RIS-based systems. Furthermore, they validate the premise that real-world deviations from ideal RIS configurations must be considered during the optimization process to ensure robust deployment.

This work is organized as follows: Section 2 describes the channel model and metrics used in the context of the discussed RIS-aided system; Section 3 details the HWIs modeling; Section 4 specifies the assumptions for the gradient coefficients computations; Section 5 discusses the results obtained from a practical experiment involving the RIS prototype; Section 6 delves into the principles behind the proposed gradient descent optimization and the RIS performance results under compensated HWIs are also analyzed, and finally, Section 7 concludes the paper.

1.1 Notation

Throughout this work, italicized letters (e.g. x or X) represent scalars, boldfaced lowercase letters (e.g. \mathbf{x}) represent vectors, and boldfaced uppercase letters (e.g. \mathbf{X}) denote matrices. The n th entry of the vector \mathbf{x} is represented by $x[n]$. The entry on the i th row and j th column of the matrix \mathbf{X} is denoted by $X_{i,j}$. The sets of real and complex numbers are represented by \mathbb{R} and \mathbb{C} , respectively. The phase content of $x \in \mathbb{C}$ is given by $\arg\{x\}$ in radians. The $\lfloor x \rfloor$ operator denotes the rounding of scalars to the nearest integer. The sets of vectors of dimension X with real and complex entries are respectively represented by \mathbb{R}^X and \mathbb{C}^X . The sets of matrices of dimension $X \times Y$ with real and complex entries are correspondingly described by $\mathbb{R}^{X \times Y}$ and $\mathbb{C}^{X \times Y}$. The transposition and conjugate transposition operations of a vector or matrix are represented as $(\cdot)^T$ and $(\cdot)^H$, respectively. The ℓ_p -norm, $p \geq 1$, of the vector \mathbf{x} is given by $\|\mathbf{x}\|_p = (|x[0]|^p + |x[1]|^p + \dots + |x[n-1]|^p)^{1/p}$. We also have $\langle \mathbf{x} \rangle = X^{-1} \sum_n x[n]$ for $\mathbf{x} \in \mathbb{R}^X$.

2 System Model

Consider a metasurface composed by passive components that can reflect the impinging electromagnetic waves. These components can be thought as varactors or varistors with adjustable impedance values, so that each component constitutes an element or reflector of a RIS. Typically the RIS reflectors are arranged in a planar of $N = N_{\text{row}}N_{\text{col}}$ reflectors (with sides of size d_H and d_V meters each), which can be represented mathematically by $\boldsymbol{\omega}_\theta = e^{j\theta} \in \mathbb{C}^N$, where $\boldsymbol{\theta} = [\theta_0, \theta_1, \dots, \theta_{N-1}]^T$. Therefore, a receiving user equipment (UE) can experience improvements in communication, whenever the signal transmitted by the access point (AP) is properly reflected by the RIS.

To elaborate, assume the baseline propagation model of Figure 1. It shows the direct channel with L_d propagation paths between the AP and UE; the composite channel is also illustrated, being composed by the channels cascade between the AP and RIS, with L_a paths, and RIS to the UE, with L_b paths (omitted from Figure 1 for better overall visibility). The direct channel is assumed to be NLOS whereas the composite channel is line-of-sight (LOS) dominated. This propagation scenario may occur when the UE is experiencing signal blocking, while the RIS is not, since it can be placed in an advantageous position for signal reflection [3, 4]. In summary, the main objective of the RIS is to change phase rotations of the signal propagating through the composite channel, in order to combine coherently at the UE the signals coming from both the direct and composite channels. More specifically, for each different path of the composite channel ($L_a L_b$ paths), N new paths are created with a modified phase-shift according to $\theta_n = [-\pi, \pi] \forall n \in N$.

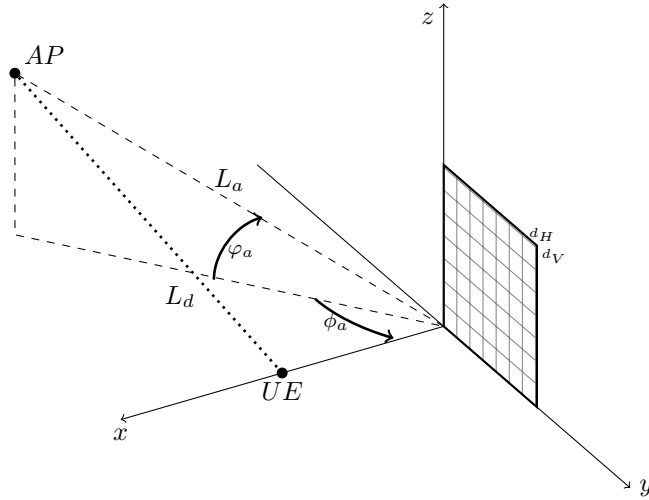


Fig. 1 Spatial diagram of the propagation model on a (x, y, z) coordinate system. Each RIS reflector has sides of size d_H and d_V meters, as illustrated.

Also illustrated in Figure 1 are the relative azimuth angles of arrival (ϕ_a) and departure (ϕ_b) at/from the RIS, as well as the respective elevation angles φ_a and φ_b (angles for the L_b channel paths are omitted given the redundant representations). These angles are used to compute the array response of the RIS reflectors as a whole. The array response dictates that the RIS reflector farthest from the plane origin imposes more rotation to the signal, with the other reflectors presenting gradually less rotation as they draw closer to the plane origin [10]. These rotation values are then weighted by the impinging signal angles, to compensate for different signal source/destination locations on the plane of Figure 1.

Furthermore, in this work we consider that signal transmission is performed over wideband communication channels, by resorting to the OFDM system. This adds to the difficulty of finding the appropriate configuration for the RIS reflectors. It is known

that there is no unique phase-shift configuration for the RIS that can simultaneously maximize the channel capacity at the UE for all K subcarriers [4]. Bear in mind that each subcarrier presents different channel phase rotations, rendering it unfeasible to configure a different $\boldsymbol{\omega}_\theta$ for each subcarrier whilst a constant RIS configuration is assumed for a given bandwidth. Therefore, to further understand the RIS configuration problem, we define the achievable rate as follows

$$R = \frac{B}{\xi} \sum_{i=0}^{K-1} \log_2 \left(1 + \frac{p_i \|\mathbf{f}_i^H \mathbf{h}_d + \mathbf{f}_i^H \mathbf{V}^T \boldsymbol{\omega}_\theta\|_2^2}{BN_0} \right) \text{ bit/s}, \quad (1)$$

wherein $\xi = K + M - 1$, to take into account the cyclic prefix loss, $\mathbf{p} \in \mathbb{R}^K$ is the power vector, with $p[k]$ being the power allocated to the k -th subcarrier, such that $P = \langle \mathbf{p} \rangle$; P being the total transmission power, \mathbf{f}_i represents the i -th row of the discrete Fourier transform (DFT) matrix $F_{i,j} = e^{-j2\pi ij/K}$, $\mathbf{h}_d \in \mathbb{C}^K$ denotes K samples (with $K - M$ padding samples) of the time domain signal transmitted through the direct channel, $\mathbf{V} \in \mathbb{C}^{N \times K}$ describes the time domain signal for all N composite channels, B is the total bandwidth occupied by K subcarriers, and finally, N_0 is the additive white Gaussian noise (AWGN) power density.

Notice in (1) that the RIS configuration has considerable influence on the degree to which a coherent or constructive combination of signals can be achieved at the UE. By letting the subcarriers power allocation be provided by the well-known water filling algorithm [5, 11], then it is easy to show that a more constructive combination of signals is directly proportional to higher values for the achievable rate of (1). In fact, a wealth of research [4, 10, 12] is available in which the optimization of the RIS configuration is investigated in the context of achievable rate maximization, for instance. However, this matter is not as straightforward when hardware impairments or imperfections prevent the RIS to function within its nominal parameters. In the next section we delve into more details about RIS hardware imperfections and propose a solution to mitigate their undesirable effects.

3 RIS Hardware Imperfections

The RIS configuration may deviate from the ideal due to a variety of hardware imperfections or impairments [7]. Typically, the RIS can be contaminated mainly by system-level noise as well as hindered by imperfections on the material that constitutes its surface, for example. Therefore, we first present the PSN model, followed by the modeling of RIS surface deformations and their consequences on the RIS configuration.

3.1 Phase-shift Noise

In this work, we employ the following modeling for the PSN impairment:

$$\hat{\boldsymbol{\omega}}_\theta = \epsilon \boldsymbol{\omega}_\theta + \mathbf{v} \sqrt{1 - \epsilon^2}, \quad (2)$$

for which $\hat{\boldsymbol{\omega}}_\theta \in \mathbb{C}^N$ represents an imperfect configuration for the RIS phase-shifts due to the PSN: $\mathbf{v} = [v_0, v_1, \dots, v_{N-1}]^T \in \mathbb{R}^N$, wherein each entry is given by

$v_n \sim \mathcal{N}(0, 1), \forall n$. More specifically, note in (2) that the uncorrelated PSN values, \mathbf{v} , are being combined with the ideal configured phase-shifts, $\boldsymbol{\omega}_\theta$, accordingly, so that $\|\hat{\omega}_{\theta_n}\|_2^2 = 1 \forall n$. In other words, the inherent passivity of the RIS reflectors remains preserved. Therefore, a wide range of PSN intensity can be investigated by adjusting $\epsilon \in \mathbb{R}$, since $\epsilon = 0$ represents the worst configuration for the RIS, whereas $\epsilon = 1$ is the ideal case where there are no imperfections.

3.2 RIS Surface Deformations

Whether the RIS planar surface is subjected to deterioration due to the environment exposure or even because of imprecisions in the manufacturing process, it can nevertheless cause a considerable negative impact on the RIS performance [7]. In this work, we consider RIS surface deformations of a regular shape, giving rise to fixed phase-shift errors for groups of reflectors. The grouped fixed phase-shift errors are given by

$$\hat{\boldsymbol{\theta}} = \boldsymbol{\theta} + \frac{2\pi}{\lambda} h_{max} \sin(k\boldsymbol{\psi}) (\cos(\varphi_a) + \cos(\varphi_b)); \text{ where} \quad (3)$$

$$\boldsymbol{\psi} = (N_{col} - 1)^{-1} [\lfloor 0/N_{col} \rfloor, \lfloor 1/N_{col} \rfloor, \dots, \lfloor N-1/N_{col} \rfloor]^T,$$

in which $\boldsymbol{\theta} \in \mathbb{R}^N$ is the ideal phase-shift configuration, also $\lambda = 3 \times 10^8 f_c^{-1}$, f_c being the central frequency of the signal carrier, h_{max} represents the maximum deformation or displacement of the RIS surface in relation to the ideal surface and k defines the number of peaks (maximum) deformations across the RIS surface. Consequently, $\boldsymbol{\omega}_{\hat{\theta}}$ represents the RIS configuration affected by the surface deformations. Figure 2 illustrates an example of the surface deformations that result from $k = \pi$ in (3).

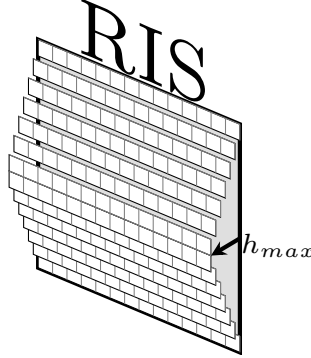


Fig. 2 RIS surface deformation (not to scale) considering $k = \pi$ in (3). Notice how grouped fixed deformations occur for all reflectors of a same (horizontal) line.

4 Gradient Computations

Suppose that the RIS is able to afford local signal processing, such as the following gradient computations

$$\nabla_{\bar{\theta}} = - \sum_{\forall i} \frac{\partial \|\mathbf{f}_i^H \mathbf{h}_d + \mathbf{f}_i^H \mathbf{V}^T \boldsymbol{\omega}'_{\theta}\|_2^2}{\partial \boldsymbol{\omega}'_{\theta}} \bigg|_{\boldsymbol{\omega}'_{\theta} = \bar{\boldsymbol{\omega}}_{\theta}}, \quad (4)$$

in which $\boldsymbol{\omega}'_{\theta} = e^{j\theta'} \in \mathbb{C}^N$ represents the RIS configuration affected by the hardware imperfections discussed in Section 3, while $\bar{\boldsymbol{\omega}}_{\theta} = e^{j(\theta' + \bar{\theta})} \in \mathbb{C}^N$ is denoted as the compensated RIS configuration. Therefore, we propose a lightweight gradient descent optimization based on the gradients computed via (4). It can be used to compute phase-shifts compensations ($\bar{\theta} \in \mathbb{R}^N$), so that the RIS hardware imperfections are locally compensated. Notice in (4) that the RIS is assumed to be channel-aware, since the gradient computations make use of channel samples \mathbf{h}_d and \mathbf{V} . In addition, the imperfect configuration, $\boldsymbol{\omega}'_{\theta}$, is also assumed to be known through the realization of RIS calibration procedures. Figure 3 brings a diagram showing the compensation of the imperfect RIS configuration from a general perspective.

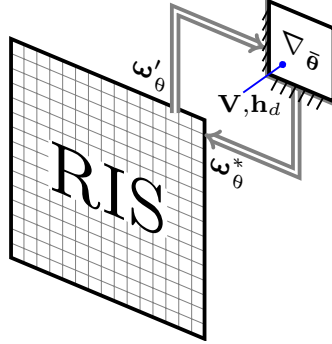


Fig. 3 Diagram illustrating the compensation of RIS hardware imperfections with the aid of gradient descent operations. The final adjusted RIS configuration is denoted by ω^*_{θ} .

The gradients computation, described symbolically in (4), is carried out by numerical methods detailed in Section 6. It can be shown that the proposed gradient descent optimization is capable of minimizing the norm magnitude of (4). Consequently, as discussed in Section 2, this is equivalent to maximizing the achievable rate at the UE with the adjusted RIS configuration ω^*_{θ} .

5 Experimental Results

Prior to presenting the numerical results obtained with computational simulations, we discuss experimental insights on the RIS electromagnetic response under surface imperfections. We briefly demonstrate in this section, that structural deformations,

whether introduced during fabrication or installation, can result in undesirable frequency responses by the RIS. The measurements were conducted in an anechoic chamber, ensuring that the RIS was tested in a multipath-free environment.

The RIS prototype used in the experiment was developed with a PET (polyethylene terephthalate) substrate that was initially covered with adhesive paper as a masking layer. The desired metasurface pattern was then engraved onto the adhesive paper using a laser cutter. After the laser engraving, the excess adhesive material was carefully removed, leaving behind a patterned mask that exposed only the regions intended for metallization. Subsequently, silver conductive paint was applied to the exposed areas with a squeegee, using a screen-printing technique. The painted substrate was then cured in an oven at 40 °C for 40 minutes to ensure proper adhesion and conductivity. Once the curing process was complete and the paint had dried thoroughly, the remaining adhesive mask was peeled away, revealing the final metasurface structure defined by the silver coating. However, it is noteworthy that due to the high power of the laser cutter, the PET substrate exhibited several surface imperfections (primarily a high roughness) caused by heat exposure.

Figure 4 illustrates the experimental setup, where we employed two horn antennas, the aforementioned RIS prototype, and a Keysight E5071C vector network analyzer (VNA) to measure the transmission coefficient S_{21} . It is well known that the scattering parameter S_{21} characterizes the forward transmission of a two-port VNA, representing the proportion of the incident signal at port 1 that is transmitted to port 2 under matched termination conditions. This parameter encompasses both the amplitude and phase of the transmitted wave and is fundamental for assessing key performance metrics such as gain, insertion loss, and overall transmission efficiency. Typically, $|S_{21}|$ is expressed in decibels (dB) using a logarithmic scale. It is also widely accepted that when S_{21} falls below -10 dB, the device under test exhibits predominantly reflective behavior, indicating poor transmission through the system [13]. Moreover, note in Figure 4 that the RIS prototype was placed at the midpoint between the antennas, which were aligned to maintain consistent polarization and minimize misalignment losses. The ETS-Lindgren 3115 double-ridge horn antenna was used at the transmission side, while a custom-designed horn antenna was employed at the reception side.

The initial step in the measurement procedure consisted of a full two-port calibration of the VNA, employing a standard calibration kit comprising of open, short, and matched load terminations. Following the calibration, the transmission coefficient S_{21} was measured with the absence of the RIS prototype between the horn antennas. This measurement was then stored in the VNA internal memory, to be used subsequently as a baseline reference. Therefore, to isolate the frequency response of the RIS, a normalization procedure was applied, in which each S_{21} measurement was divided by the aforementioned baseline measurement. This operation is performed using the VNA and effectively centers the resulting S_{21} curves around 0 dB, as shown in Figure 5. Consequently, systematic measurement variations, path loss, and antennas response are compensated accordingly. Bear in mind that the S_{21} measurement, after this calibration process, constitutes only of the measurement obtained from the RIS prototype under evaluation.

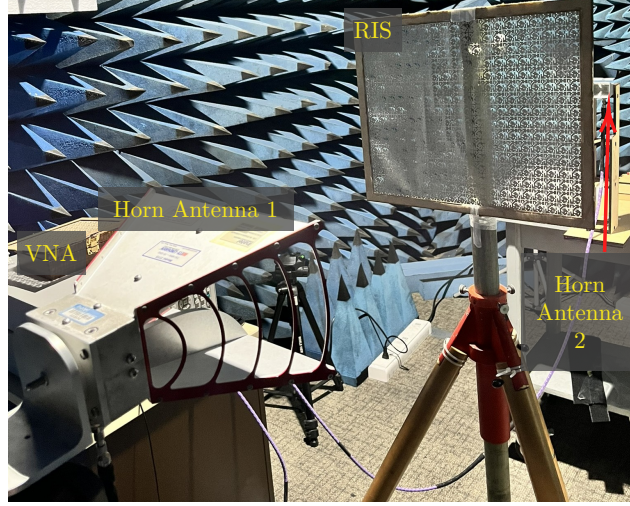


Fig. 4 Photography of the experimental setup.

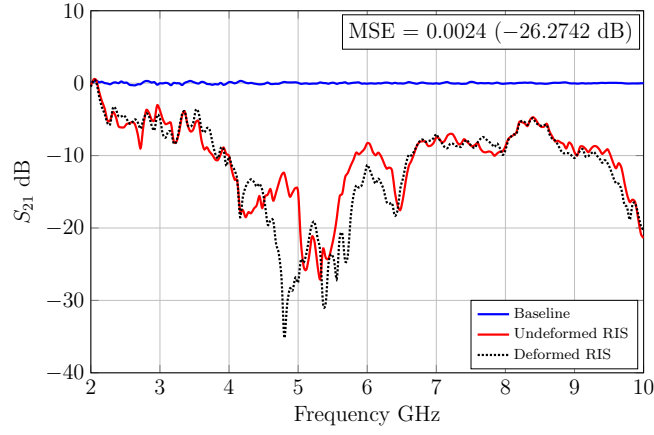


Fig. 5 Measured transmission coefficient S_{21} for the undeformed and deformed RIS, highlighting the impact of structural modifications on the RIS.

Following the calibration process, the RIS was positioned between the two horn antennas to acquire its S_{21} measurement over the frequency range of 2 to 10 GHz. Figure 5 shows the results, where the S_{21} measurement of the undeformed RIS indicates its expected reflective behavior across nearly the entire frequency range. Additionally, the S_{21} measurement for the deformed RIS is also illustrated in Figure 5. For the deformed RIS measurements, a structural deformation was introduced at the center of the RIS, by using a dielectric material to create a localized surface displacement. This resulted in a surface curvature of approximately 1 cm (e.g. 0.1λ for 3 GHz), simulating structural deformations that may arise from environmental factors

or installation processes. As observed in Figure 5, the deformation leads to a measurable deviation from the obtained with the undeformed RIS. More precisely, one can verify a deviation with a mean squared error (MSE) of 0.0024 or, correspondingly, of -26.27 dB between the deformed and undeformed measurements. Therefore, these results highlight the sensitivity of the RIS performance to HWIs. In other words, the measured S_{21} magnitude revealed noticeable changes across the frequency spectrum when there is even a slight deformation on the RIS surface. This confirms that even minor material variations can cause significant perturbations in the RIS response, which, if not accounted for, may degrade the system performance.

6 Numerical Results

As stated in Section 4, we leverage numerical methods for computing the gradients that are employed in the gradient descent optimization. In the following, we discuss how the optimization is carried out. Furthermore, the compensated RIS configuration provided by the proposed gradient descent optimizer is evaluated using computational simulations.

However, let us first specify all relevant system model parameters, since they are used throughout this section: (i) the $L_a = 101$ path delays $\tau_a^l \sim \mathcal{U}[\tau_a^1, 2\tau_a^1]$, $\forall l > 1$, have their first path, $l = 1$, as the strongest LOS path (same apply for the $L_b = 51$ path delays τ_b^ℓ); (ii) all $L_d = 100$ path delays obey $\tau_d^l \sim \mathcal{U}[\tau_d, 2\tau_d]$, where τ_d is the time, in seconds, that the signal takes to propagate from the AP to the UE (LOS path); (iii) the azimuth and elevation angles of arrival/departure considered for the RIS can vary randomly around the LOS path initial angle, with $\phi_{a,b} \sim \mathcal{U}[-40^\circ, 40^\circ]$ and $\varphi_{a,b} \sim \mathcal{U}[-10^\circ, 10^\circ]$; (iv) also let $f_c = 3$ GHz, $B = 10.5$ MHz and $N_0 = -164$ dBm; and, finally, (v) we assume for each RIS reflector that $d_H = d_V = 0.25\lambda$ meters. We moreover refer the interested readers to [10] for further details about the channel model specifications.

6.1 Gradient Descent Optimizer

In this work, we employ the so-called automatic differentiation in order to compute the gradients expressed in (4). More specifically, we use the computational tools provided by the TensorFlow platform [14]. With the gradients computed by the automatic differentiation, then the phase-shift compensation, $\bar{\boldsymbol{\theta}}$, is updated in the following manner:

$$\bar{\boldsymbol{\theta}}_k = \bar{\boldsymbol{\theta}}_{k-1} - \gamma \nabla_{\bar{\boldsymbol{\theta}}}, \quad (5)$$

where $k = [1, 2, \dots, K]^T$ and γ roughly controls by how much, or how fast, is the descent to local minima of (4); it is usually referred to as the learning rate. This update operation is repeated until the stopping criteria is met or if the maximum number of iterations, K , is reached.

The gradients update shown in (5) is one of the simplest form of computing the gradient descent, with more sophisticated alternatives such as the ADAM optimizer being also available. For readers interested in an comprehensive discussion of different optimizations methods, see [15] and the references therein. We nevertheless briefly

show that the RIS hardware imperfections can be compensated more efficiently with the simple update given by (5).

Let us first introduce the strongest tap maximization (STM) [4, 10] method for configuring the RIS:

$$\boldsymbol{\omega}_\theta^{(m^*)} = \arg \max_{m \in \{0,1,\dots,M-1\}} \|h_d[m] + \mathbf{V}_m^T \boldsymbol{\omega}_\theta^{(m)}\|_2^2, \quad (6)$$

where \mathbf{V}_m is the m -th column of \mathbf{V} and also

$$\boldsymbol{\omega}_{\theta_n}^{(m)} = e^{j(\arg\{h_d[m]\} - \arg\{V_{m,n}\})}, \quad \forall n \in \{0,1,\dots,N-1\}, \quad (7)$$

which represents the alignment of phase-shifts for all N RIS elements, such that the direct channel, \mathbf{h}_d , combines in-phase with the composite channel, \mathbf{V} , for the m -th time sample. Therefore, in this work we assume that the STM is the ideal phase-shift RIS configuration as intended by the AP. However, from Section 3, we know that this configuration is not going to be ideally represented by the RIS reflectors.

With that in mind, observe in Figure 6 that the relative rate¹ obtained from the optimization of a imperfect STM configuration, is traced for the average number of gradient update iterations (with $\gamma = 10^{-2}$). The ideal STM configuration performance and the PSN effect on its performance is also illustrated in Figure 6, alongside the results obtained with a random compensator². Consequently, note that both the gradient descent and ADAM optimizers improve their performances as the number of iterations increases, whilst the performances for the STM and random compensator are fixed, as expected. The objective of the optimizers is to compensate for hardware imperfections (see Section 4), so that it can be seen in Figure 6 that after ~ 25 iterations the optimizers are able to reach the ideal STM configuration performance. In fact, the ADAM optimizer can be even employed in the RIS configuration by itself (Figure 6 (b)), that is, with no initialization from the STM configuration ($\boldsymbol{\omega}'_\theta = \hat{\boldsymbol{\omega}}_\theta$ since only the PSN is present). In conclusion, although the updates of (5) do not offer the most robust optimizer performance, yet for the task at hand, that is, hardware imperfections compensation, it is equivalent to the ADAM optimizer. Since the complexity of the ADAM is greater [15] for each iteration, thus the simple gradient descent update of (5) is used for the remainder of this work.

6.2 Performance Evaluation

In this subsection we evaluate the performance of the gradient descent optimizer, utilizing the gradients update operation given by (5). Figure 7 shows the relative rate performance with the optimizer, in comparison to the ideal performance obtained with the STM configuration of a perfect RIS. Moreover, Figure 7 illustrates the STM configuration performance considering the hardware imperfections discussed in Section 3, that is, the PSN of (2) and the RIS surface deformations of (3). It is worth noting

¹The relative rate is the ratio between the achievable rate obtained with perfectly coherent combination, and the actual achievable rate [10].

²We assume a random compensator phase $\bar{\boldsymbol{\theta}} \sim \mathcal{U}[-\pi, \pi]$, instead of the one computed by the optimizer, as a lower bound for performance.

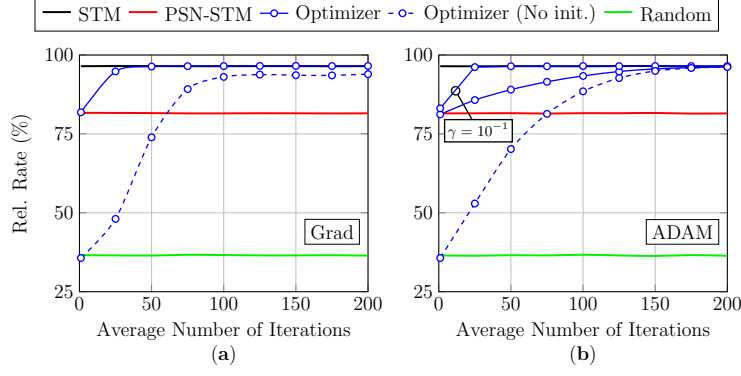


Fig. 6 Relative rate performance of the gradient descent ('Grad') and ADAM optimizers, in comparison to the ideal/uncompensated STM configurations for the RIS. Each simulation point employed up to 5×10^3 Monte Carlo runs.

that the optimizer compensates the RIS configuration under the combined effect of the aforementioned hardware imperfections. Note also that the random configuration is presented in Figure 7, being a lower bound to the relative rate performance. Finally, we assume $\rho = 0.5$ in (2), $h_{\max} = 0.1\lambda$ [7] and $k = \pi$ in (3). The LOS path initial angle is such that $\varphi_{a,b} = 0^\circ$; we also employ $K = 700$ subcarriers and a range of RIS sizes (N).

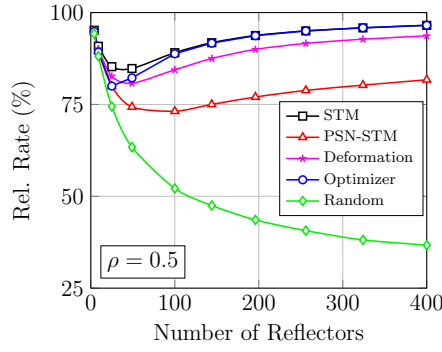


Fig. 7 Relative rate performance for the optimizer (5), considering the STM affected by the PSN (2) and also by the RIS surface deformations (3), with the ideal STM (6) as a upper bound reference and the random configuration as the lower bound. Each simulation point employed 10^3 Monte Carlo runs.

Therefore, observe in Figure 7 that the optimizer is able to totally compensate the hardware imperfections of RISs with 100 reflectors or more. Despite the considerable drop in performance due to the PSN, the RIS deformations on the other hand are not as impactful. Consequently, in Figure 8 we evaluate the relative rate performance for $k = 2\pi$ in (3), also with $\rho = 0.5$ (Figure 8 (a)), $\rho = 0.1$ (Figure 8 (b)) and $\rho = 0$ (Figure 8 (c)), while other parameters are kept the same. It is shown in [7] that increasing k can lead to beamforming shapes that are detrimental to the general RIS performance.

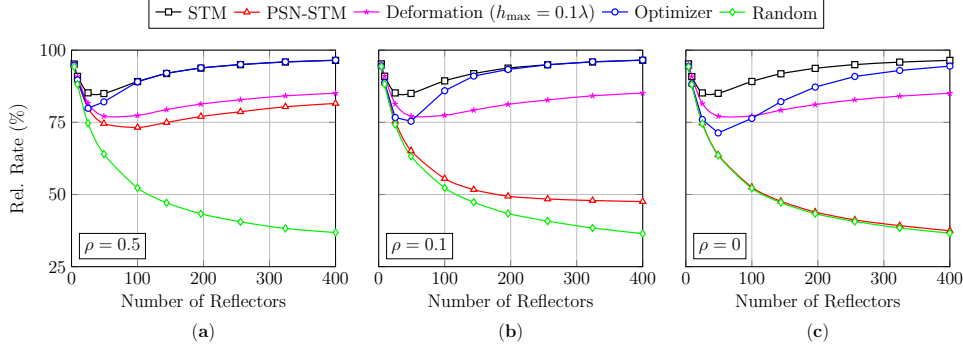


Fig. 8 Relative rate performance for the optimizer (5), now compensating for the combined hardware imperfections considering RIS surfaces deformations with $k = 2\pi$ in (3). Also, $\rho = 0.5$ (a), $\rho = 0.1$ (b) and $\rho = 0$ (c) in (2) are evaluated. Each simulation point employed up to 5×10^3 Monte Carlo runs.

Therefore, verify in Figure 8 (a) that increasing the number of deformation peaks, k , also worsens the relative rate performance. We conjecture that this happens because higher values of k translates to more phase-shift discrepancy between adjacent groups of RIS reflectors. This in turn will lead to more phase misalignment at the UE, consequently reducing the achievable rate. Note also in Figures 8 (b)-(c) that the increase in the PSN intensity can lead to prohibitive performances by the STM configuration for the RIS. Nevertheless, the optimizer is still able to compensate satisfactorily for the combined hardware imperfections. See in Figure 8 (c) that even with the fully uncorrelated PSN, the optimizer can reach the ideal STM performance for a RIS with $N = 400$ reflectors. Additionally, Figure 9 shows the relative rate performance changes caused by only increasing the magnitude of deformation peaks to $h_{\max} = 0.2\lambda$. As reported in [7], for $k = 2\pi$, values of $h_{\max} > 0.1\lambda$ can lead to significant loss of beamforming performance. This is also true for the relative rate performance, specially when the combined hardware imperfections are evaluated, as in Figures 9 (a)-(c). Yet note that the optimizer is able to compensate these severe hardware imperfections, reaching the ideal STM performance for $N = 400$ reflectors.

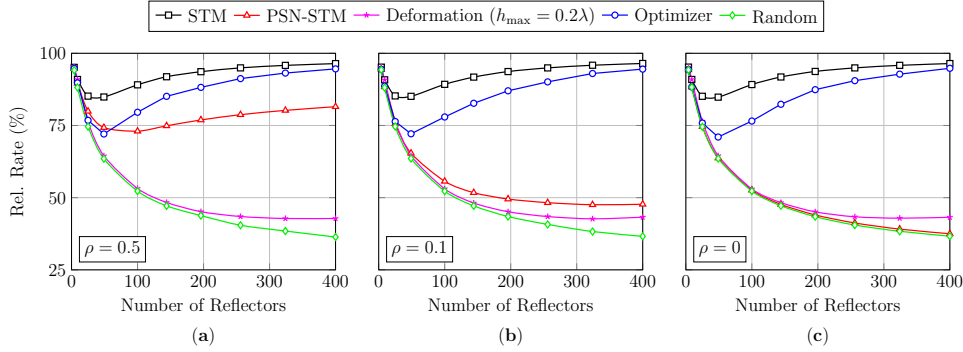


Fig. 9 Relative rate performance for the optimizer (5), now considering RIS surfaces deformations with peaks magnitudes defined by $h_{\max} = 0.2\lambda$ in (3). Each simulation point employed up to 5×10^3 Monte Carlo runs.

7 Conclusions

In this work we discussed the effects of RIS HWIs in the context of signal transmission over wideband communication channels assisted by RIS systems. More importantly, we demonstrated that by leveraging the gradient descent optimization, it is possible to compensate for the PSN and RIS surface deformations, consequently mitigating the loss of performance associated with these HWIs. The proposed gradient descent optimization is fully numerical and is based on the automatic differentiation for computing the gradient coefficients. It was also shown that this approach does not require a priori knowledge of the HWIs average behavior and distributions.

For future works, more results from diverse practical experiments involving the RIS, can pave the way for precise HWIs characterizations. This can be conducive for the development of RISs hardware that are more robust in real deployment scenarios.

Acknowledgements. This work was partially funded by project XGM-AFCCT-2024-2-15-1 funded by xGMobile – EMBRAPII Inatel Competence Center on 5G and 6G Networks, with financial resources from the PPI IoT/Manufatura 4.0 from MCTI grant number 052/2023, signed with EMBRAPII; by the Samurai Project funded by FAPESP (Grant No. 20/05127-2); by FAPEMIG under the contract No PPE-00124-23; and by CNPq-Brasil. The author also thank the Calibration and Testing Laboratory of Inatel (Laboratório de Ensaios de Calibração) for providing access to the anechoic chamber for the validation tests of the RIS.

Declarations

Conflict of interest. The authors declare that they have no competing interests.

References

- [1] Åström, M., Gentner, P., Haliloglu, O., Makki, B., Tagerman, O.: RIS in Cellular Networks – Challenges and Issues (2024). <https://arxiv.org/abs/2404.04753>
- [2] Alexandropoulos, G.C., Stylianopoulos, K., Huang, C., Yuen, C., Bennis, M., Debbah, M.: Pervasive machine learning for smart radio environments enabled by reconfigurable intelligent surfaces. *Proceedings of the IEEE* **110**(9), 1494–1525 (2022) <https://doi.org/10.1109/JPROC.2022.3174030>
- [3] Liaskos, C., Mamatras, L., Pourdamghani, A., Tsioliaridou, A., Ioannidis, S., Pitsillides, A., Schmid, S., Akyildiz, I.F.: Software-Defined Reconfigurable Intelligent Surfaces: From theory to end-to-end implementation. *Proc. IEEE* **110**(9), 1466–1493 (2022) <https://doi.org/10.1109/JPROC.2022.3169917>
- [4] Björnson, E., Wymeersch, H., Matthiesen, B., Popovski, P., Sanguinetti, L., Carvalho, E.: Reconfigurable Intelligent Surfaces: A signal processing perspective with wireless applications. *IEEE Signal Process. Mag.* **39**(2), 135–158 (2022) <https://doi.org/10.1109/MSP.2021.3130549>

- [5] Yang, Y., Zheng, B., Zhang, S., Zhang, R.: Intelligent reflecting surface meets OFDM: Protocol design and rate maximization. *IEEE Trans. Commun.* **68**(7), 4522–4535 (2020) <https://doi.org/10.1109/TCOMM.2020.2981458>
- [6] Wang, R., Yang, Y., Makki, B., Shamim, A.: A wideband reconfigurable intelligent surface for 5g millimeter-wave applications. *IEEE Transactions on Antennas and Propagation* **72**(3), 2399–2410 (2024) <https://doi.org/10.1109/TAP.2024.3352828>
- [7] Yang, J., Chen, Y., Cui, Y., Wu, Q., Dou, J., Wang, Y.: How practical phase-shift errors affect beamforming of reconfigurable intelligent surface? *IEEE Transactions on Communications* **71**(10), 6130–6145 (2023) <https://doi.org/10.1109/TCOMM.2023.3293859>
- [8] Yue, C., Tang, H., Chai, L.: Fast beamforming for irs assisted multi-user communication systems by lightweight unsupervised learning. *IEEE Transactions on Vehicular Technology* **73**(11), 17180–17191 (2024) <https://doi.org/10.1109/TVT.2024.3427001>
- [9] Huang, S.-Y., Lin, J.-Y., Wang, C.-Y., Hwang, R.-H.: Mse minimization for ris-assisted wireless networks with phase error and phase-dependent amplitude response. In: 2024 IEEE 99th Vehicular Technology Conference (VTC2024-Spring), pp. 1–6 (2024). <https://doi.org/10.1109/VTC2024-Spring62846.2024.10683024>
- [10] Souza, P.H.C., Khazaei, M., Leonel Mendes, L.: Resource-efficient configuration of RIS-aided communication systems under discrete phase-shifts and user mobility. *IEEE Transactions on Communications* **73**(1), 145–157 (2025) <https://doi.org/10.1109/TCOMM.2024.3432690>
- [11] Bjornson, E., Zetterberg, P., Bengtsson, M., Ottersten, B.: Capacity limits and multiplexing gains of MIMO channels with transceiver impairments. *IEEE Commun. Lett.* **17**(1), 91–94 (2013) <https://doi.org/10.1109/LCOMM.2012.112012.122003>
- [12] Feng, B., Gao, J., Wu, Y., Zhang, W., Xia, X.-G., Xiao, C.: Optimization techniques in reconfigurable intelligent surface aided networks. *IEEE Wirel. Commun.* **28**(6), 87–93 (2021) <https://doi.org/10.1109/MWC.001.2100196>
- [13] Pozar, D.M.: *Microwave Engineering: Theory and Techniques*. John Wiley & Sons, Hoboken, New Jersey (2021)
- [14] Abadi, M., Barham, P., Chen, J., Chen, Z., Davis, A., Dean, J., Devin, M., Ghemawat, S., Irving, G., Isard, M., Kudlur, M., Levenberg, J., Monga, R., Moore, S., Murray, D.G., Steiner, B., Tucker, P., Vasudevan, V., Warden, P., Wicke, M., Yu, Y., Zheng, X.: TensorFlow: A system for large-scale machine learning (2016). <https://arxiv.org/abs/1605.08695>

- [15] Zappone, A., Di Renzo, M., Debbah, M.: Wireless networks design in the era of deep learning: Model-based, AI-based, or both? *IEEE Transactions on Communications* **67**(10), 7331–7376 (2019) <https://doi.org/10.1109/TCOMM.2019.2924010>



Pedro H. C. de Souza was born in Santa Rita do Sapucaí, Minas Gerais, MG, Brazil in 1992. He received the B.S., M.S. and the Doctor degrees in telecommunications engineering from the National Institute of Telecommunications - INATEL, Santa Rita do Sapucaí, in 2015, 2017 and 2022, respectively; is currently working as a postdoctoral researcher in telecommunications engineering at INATEL, with the support of FAPESP (*Fundação de Amparo à Pesquisa do Estado de São Paulo*). During the year of 2014 he was a Hardware Tester with the INATEL Competence

Center - ICC. His main interests are: digital communication systems, mobile telecommunications systems, 6G, reconfigurable intelligent surfaces, convex optimization for telecommunication systems, compressive sensing/learning, cognitive radio.



Luiz A. M. Pereira received the B.Sc., M.Sc., and Ph.D. degrees in Telecommunications from the National Institute of Telecommunications (Inatel), Brazil, in 2017, 2020, and 2023, respectively. He has acted as a researcher at the Wireless and Optical Convergent Access (WOCA) and Reference Center in Radiocommunications (CRR) laboratories, working on Brasil 6G and xGMobile Projects. Since 2024, he is a professor at Inatel.



Faustino Reyes Gómez received his B.Sc., M.Sc., and Ph.D. in Physics from Universidad del Valle in Cali, Colombia. He is currently a postdoctoral researcher at the National Telecommunications Institute (Inatel). His main research areas include the design and simulation of nanophotonic systems for biosensing applications, as well as the design, simulation, and development of metasurfaces for use in 5G and 6G telecommunications. He also has teaching experience, having served as a teaching assistant and

full-time professor in various physics courses.



Elsa Maria Materón holds a degree in Chemistry from Universidad del Valle (Colombia), where she excelled in her work on condensed matter physics. She earned both her Master's and Ph.D. in Biotechnology from São Paulo State University (UNESP). During her doctoral studies, she completed research internships at the Institute for Nanotechnology at the University of Waterloo (Canada), focusing on the SELEX process for aptamer synthesis and the development of enzymatic biosensors for studying chemotherapeutic drugs. Additionally, she was a visiting student at the University of Pennsylvania (USA), where she worked on graphene-based field-effect transistors and the synthesis of graphene via CVD. She completed postdoctoral fellowships at the Federal University of São Carlos (UFSCar), the University of Pennsylvania (Department of Physics and Astronomy), the Institute of Physics of São Carlos (IFSC-USP), the Institute of Chemistry of São Carlos (IQSC-USP), and the Graphene and Nanomaterials Research Center (MackGraphe). She is a researcher at the National Institute of Telecommunications (Inatel) and a collaborator at IFSC. Her research focuses on developing electrochemical and optical sensors and biosensors for clinical diagnostics, microfluidic devices, microfabrication, and antenna and metasurface fabrication. She possesses extensive experience in nanomaterial synthesis, biogenic nanoparticles, Langmuir films, and the physicochemical characterization of surfaces.



Jorge Ricardo Mejía-Salazar obtained his B.Sc., M.Sc., and Ph.D. degrees in Physics from Universidad del Valle in Cali, Colombia, in 2008, 2009, and 2014, respectively. After completing his Ph.D., he pursued postdoctoral research at the Institute of Physics, Federal University of Alagoas, Maceió, Brazil (2014–2016), and later at the São Carlos Institute of Physics, University of São Paulo, Brazil (2016–2018). Since 2018, Jorge has been a Professor at the National Institute of Telecommunications (Inatel) in Santa Rita do Sapucaí, Minas Gerais, Brazil. His research interests include applied electromagnetism, reconfigurable intelligent surfaces (RIS), antennas, nanoantennas, and the electromagnetic principles governing chiral, magneto-chiral, magneto-optic, and magnetoplasmonic effects in nanostructures.



Luciano Leonel Mendes received the B.Sc. and M.Sc. degrees from Inatel, Brazil, in 2001 and 2003, respectively, and the Doctor degree from Unicamp, Brazil, in 2007, all in electrical engineering. Since 2001, he has been a Professor with Inatel, where he has acted as the Technical Manager of the Hardware Development Laboratory from 2006 to 2012. From 2013 to 2015, he was a Visiting Researcher with the Technical University of Dresden in the

Vodafone Chair Mobile Communications Systems, where he has developed his post-doctoral. In 2017, he was elected Research Coordinator of the 5G Brazil Project, an association involving industries, telecom operators, and academia which aims for funding and build an ecosystem toward 5G in Brazil. He is also the technical coordinator of the Brazil 6G Project.